PCCP

ROYAL SOCIETY OF CHEMISTRY

PAPER

View Article Online
View Journal | View Issue

Cite this: *Phys. Chem. Chem. Phys.*, 2024, **26**, 4011

Wide-angle camouflage detectors by manipulating emissivity using a non-reciprocal metasurface array

Bowei Zhang,[a] Bin Wang[a] and Sandeep Kumar Chamoli *[bc]

Received 20th October 2023,
Accepted 14th December 2023

DOI: 10.1039/d3cp05097a

rsc.li/pccp

Camouflage detectors that can detect incoming radiation from any angle without being detected are extremely important in stealth, guided missile, and heat-seeking missile industries. In order to accomplish this, the absorption and emission processes must be manipulated simultaneously. However, Kirchhoff's fundamental law suggests that absorption and emission are always in the same direction $\alpha(\theta) = \varepsilon(\theta)$, *i.e.*, absorption and emission are reciprocal. This means that the emission from the detector always points back to the source, for example towards a laser source in a guided missile. Thus, detector emission serves as a complementary measure to hide an object. Here, we present a novel camouflage detector that uses a nonreciprocal metasurface array to independently detect the direction of the incoming radiation as well as manipulate its emissivity response. This is accomplished by using a magneto-optical material called indium arsenide (InAs), which breaks Lorentz reciprocity and Kirchhoff's fundamental law such that $\alpha(\theta) \neq \varepsilon(\theta)$. This design results in the following absorption and emission: $\alpha(\theta) = \varepsilon(-\theta)$. Nine metasurfaces were designed, optimized, and operated at different incident angles from $+50^\circ$ to -50° at a wavelength of 13 μm. Furthermore, by keeping all metasurfaces in a pixilated array form, one could make a device that works over the full $\pm 50^\circ$ range. Potentially, this array of nonreciprocal metasurfaces can be used to fabricate thermal emitters or solar-harvesting systems.

1. Introduction

Radiation is an omnipresent special phenomenon in which heat transfer does not require a medium.[1–3] Maxwell's theory predicts the radiative properties of an object and Planck's theory predicts the amount of radiation emitted by a body at a particular wavelength.[4–6] Owing to the omnipresence of radiation, they are a central attraction for many science and engineering applications such as energy conversion,[7,8] imaging,[9–11] sensing[12] and infrared (IR) camouflage technology.[13,14] Owing to its importance in both civil and military applications, IR camouflage has received considerable attention. IR camouflage technology conceals the infrared signature of objects so that they cannot be detected by IR-based devices, such as thermal imaging systems, heat-seeking missiles, or IR missile warning satellites.[15–18] Because all surfaces above absolute zero emit and receive radiation, it is challenging to hide the target thermal radiation using thermal camouflage. According to thermodynamic laws, the radiation of an object is directly proportional to its surface emittance (ε) and temperature (T). It can be concluded that IR thermal camouflage can be attained either by controlling the surface emission (radiative camouflage) or surface temperature (conduction thermal camouflage). For practical purposes, radiation camouflage is more promising because the radiative properties can be modulated based on the surface characteristics, whether they are flattened, curved, smooth, rough or flexible.[19–22] It is possible to modulate the spectral, spatial, and polarization characteristics of thermal radiation,[23–35] using nanostructures such as photonic crystals, gratings, multi-layered structures, meta-materials, and metasurfaces. For all proposed nanophotonic camouflage designs, emissivity is required to be near zero in the atmospheric window (8 μm to 14 μm), which is transparent to radiation and prone to detection.[4,5] Recently, Chamoli *et al.* proposed the use of phase change materials[36,37] to control emissivity in two different phases through reconfigurable radiative metasurface designs[38–41] Kirchhoff's law is the governing principle of thermal emission, which dictates that all objects have equal emission and absorption, or more precisely, they follow Lorentz reciprocity.[4,42] All of the previously proposed nanophotonics camouflage designs comply with this law. However, this law is not valid once the reciprocity has been broken in a system,[32,35] and it is now possible to produce a nonreciprocal thermal emitter that contrasts emissivity

[a] *Chongqing College of Electronic Engineering (CQCEE), Chongqing 401331, China*
[b] *Changchun Institute of Optics, Fine Mechanics and Physics, Chinese Academy of Sciences, China. E-mail: chamolisandeep28@gmail.com*
[c] *Nanyang Technological University, Singapore*

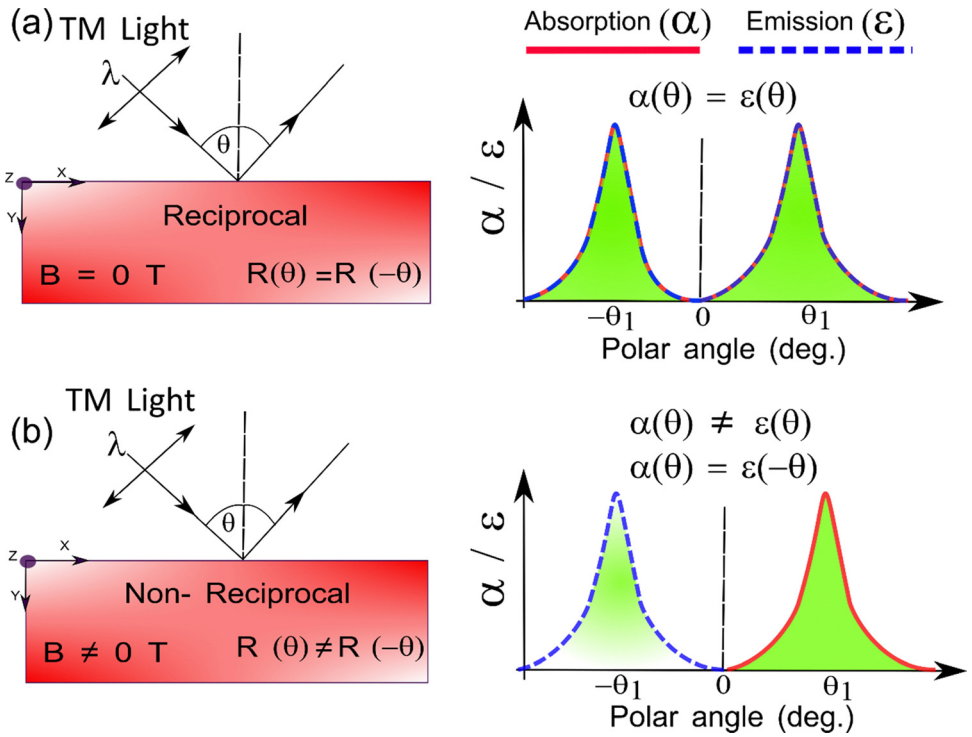

Fig. 1 Principle and comparison of (a) reciprocal and (b) non-reciprocal metasurface radiation angle detector and camouflage. With a reciprocal angle detector, *i.e.*, without an external magnetic field (B = 0 T), the resonance is symmetric with respect to the polar angle $\theta = 0^\circ$. In the resonance condition, the absorption (red solid line) and emission (blue dotted line) curves overlap each other perfectly at $+\theta_1$ and $-\theta_1$ and $R(+\theta) = R(-\theta)$. However, with a nonreciprocal angle sensor (when $B \neq 0$ T), the resonance conditions are asymmetric with respect to $\theta = 0^\circ$ and the absorption at $+\theta_1$ and $-\theta_1$ is no longer the same and $R(+\theta) \neq R(-\theta)$. $\alpha(\theta) = \varepsilon(-\theta)$ holds, meaning that if the absorption angle is $+\theta$, then the emission angle would be $-\theta$. Hence, by employing the nonreciprocity in the angle sensor, the emission is not directed toward the source, something that is not possible with a reciprocal sensor. This allows the detector to be camouflaged.

and absorptivity.[43] A nonreciprocal thermal emitter was designed by utilizing the magneto-optical effect, a technique that has been widely used to design nonreciprocal systems in the past.[44–47] Because of the unique properties of non-reciprocity, nanophotonic designs made of magneto-optical materials can potentially be used for camouflage to manipulate the emission. Additionally, because the emission window is still in the atmospheric transmission window, it can facilitate better thermal management.

Fig. 1 shows a schematic of a reciprocal and nonreciprocal angle detector and its advantage of camouflaging the detector. Non-reciprocal thermal emission has gained considerable attention after the seminal work on violating Kirchhoff's law using a photonic crystal.[45] According to Kirchhoff's law,

$$\alpha(\omega,\theta,\varphi) = \varepsilon(\omega,\theta,\varphi)$$

where α and ε are the spectral directional absorption and emission given by θ and φ, respectively. This in turn suggests that, according to the detailed balance, if an absorber absorbs light from the source, it must radiate the light back to the source. This is because of the inherent loss mechanism, which can only be eliminated by violating the detailed balance to the maximum degree. As shown in Fig. 1(a), in the reciprocal case, for a fixed wavelength, the emission and absorption angles are the same at $\pm\theta$. Therefore, if light incident from θ_1 or $-\theta_1$ has the same reflection direction along with the same absorption and emission with the same resonance wavelength or emission wavelength, *i.e.*, $R(\theta_1) = R(-\theta_1)$ and $\alpha(\theta) = \varepsilon(\theta)$. However, theoretically, nonreciprocal materials, such as magneto-optical materials, may not satisfy the detailed balance, and hence $R(\theta_1) \neq R(-\theta_1)$. Consequently, the emission and absorption angles were not the same $\alpha(\theta) \neq \varepsilon(\theta)$, as shown in Fig. 1(b) and $\alpha(\theta) = \varepsilon(-\theta)$. Therefore, we have been able to modify the emissions because of nonreciprocity in the system, and the emissions do not return to the source. Also, the absorption was not symmetric with respect to the polar angle $\theta = 0^\circ$.

In this study, we propose a metasurface that is nonreciprocal and can be used both as an all-angle detector and without being detected or camouflaged. Camouflage is the property of nonreciprocal metasurfaces to redirect emission, not to the source and detector, and is due to its ability to detect the direction of incoming light in the incident plane over the entire range from θ to $-\theta$. The magneto-optic material of choice was indium arsenide (n-InAs). To make a device work in a broad angular range, we proposed an array of metasurface optimized for different angles of incidence from $+50^\circ$ to -50°. Therefore, we designed a series of metasurfaces that can target a specific angle. By combining all the metasurfaces into an array or a pixilation form, we proposed a device that can operate in the range of $\pm 50^\circ$, which can indicate the direction of incoming radiation. As shown in Fig. 2(a), in the case of a reciprocal

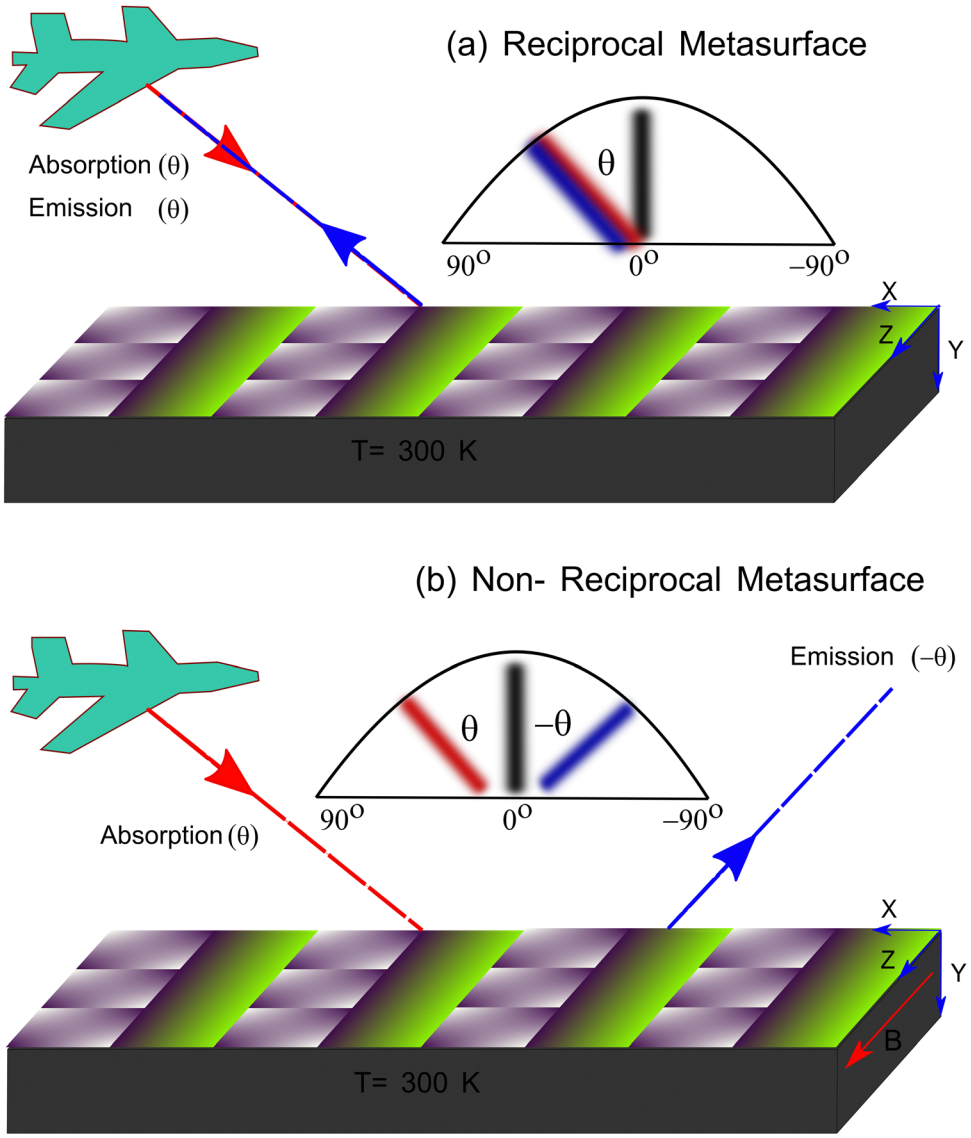

Fig. 2 Diagram of reciprocal and nonreciprocal metasurface arrays showing absorption (θ) and emission (θ) directions under an external magnetic field (red arrow in the +z-direction). (a) The nonreciprocal metasurface redirects emitted light in different directions (not back to the source), but in the (b) reciprocal metasurface case, the emission is back to the source and it cannot be employed as camouflage. Additionally, the non-reciprocal metasurface can also work as a detector by indicating the direction of the incident light as it can efficiently distinguish $+\theta$ and $-\theta$. The system can potentially be designed to operate over a broad range of angles by designing each pixel to target a specific angle.

metasurface array, the emission returns to its source, for instance, the laser light source from a missile system seeking its target. Therefore, the missile system can locate the target and hit it because of the return emission. However, in the case of a non-reciprocal metasurface array for the entire range of angles, the emission is different from the source and is therefore not detectable, as shown in Fig. 2(b). Thus, an array of this type can be used to track incoming radiation and identify its direction without being detected.

The atmospheric transmission window from 8 μm to 14 μm is the wavelength of interest because the atmosphere has low absorption and high transparency in this range. However, atmospheric transmission varies with the angle and is less transparent at higher angles.[48] The IR detector must operate within these atmospheric windows in order to detect and track aircraft used in anti-aircraft missiles.[49] We optimized all metasurfaces at 13 μm. Ideally, one can create such an array for any wavelength by using a magneto-optic material[44,45,50] and a Wyel semimetal.[51,52] Indium arsenide (InAs) exhibits exceptional magneto-optical properties under a magnetic field, which is crucial for breaking Lorentz reciprocity. This anisotropic behavior stems from the selective influence of the magnetic field on the dielectric constants in the material's x–y plane, leading to a refractive index asymmetry between the forward and backward light propagation. Notably, the refractive index in the z-direction remains unaffected. The magneto-optical characteristics of InAs enable controlled refractive index manipulation, making it invaluable for applications requiring nonreciprocal

responses, as demonstrated in our study. The magneto-optic effect becomes stronger when the off-diagonal terms ε_{xy} and diagonal terms ε_{xx} in the permittivity tensor below the magneto-optic material have a very high ratio $\frac{|\varepsilon_{xy}|}{|\varepsilon_{xx}|}$. The non-reciprocity results from $\varepsilon_{xy} = \varepsilon_{yx}$:

$$\varepsilon = \begin{pmatrix} \varepsilon_{xx} & \varepsilon_{xy} & 0 \\ -\varepsilon_{yx} & \varepsilon_{yy} & 0 \\ 0 & 0 & \varepsilon_{zz} \end{pmatrix}$$

2. Simulation methods

In order to simulate the magneto-optical effect, we used Lumerical's finite difference time domain (FDTD), which comprises three steps. The first is the introduction of anisotropic materials. The permittivity tensor can be expressed as follows:

$$\varepsilon = \begin{pmatrix} \varepsilon_{xx} & \varepsilon_{xy} & \varepsilon_{xz} \\ \varepsilon_{yx} & \varepsilon_{yy} & \varepsilon_{yz} \\ \varepsilon_{zx} & \varepsilon_{zy} & \varepsilon_{zz} \end{pmatrix} \quad (1)$$

The magneto-optic effect occurs when the direction of the magnetization vector is perpendicular to the incidence or reflection plane. In our analysis, we assume that the incident plane wave propagates along the *Y*-axis and that it is polarized along the *X*-axis. Therefore, the magnetization vector is in the *Z*-direction, and the permittivity tensor due to the symmetry of C_4 remains invariant with rotation about the *Z*-axis.

$$\varepsilon' = C_4^{-1}\varepsilon C_4 \begin{pmatrix} \varepsilon_{yy} & -\varepsilon_{yx} & -\varepsilon_{yz} \\ -\varepsilon_{xy} & \varepsilon_{xx} & \varepsilon_{xz} \\ -\varepsilon_{zy} & \varepsilon_{zx} & \varepsilon_{zz} \end{pmatrix} \quad (2)$$

Under the influence of an external magnetic field, the permittivity tensor of InAs becomes

$$\varepsilon = \begin{pmatrix} \varepsilon_{xx} & \varepsilon_{xy} & 0 \\ -\varepsilon_{xy} & \varepsilon_{xx} & 0 \\ 0 & 0 & \varepsilon_{zz} \end{pmatrix} \quad (3)$$

However, adding an anisotropic material to the database of the Lumerical diagonalization of the permittivity tensor requires calculating the eigenvalues and the unitary transformation matrix:

$$\varepsilon_{\text{diag}} = U\varepsilon U^{\dagger} \quad (4)$$

where U is the unitary matrix, $U^{\dagger}$ is the complex conjugate transpose of U and $\varepsilon_{\text{diag}}$ is a diagonal matrix. $U = V^{\dagger}$, where V is the the eigenvector matrix of ε. $\varepsilon_{\text{diag}}$ needs to be added to the material database. The second step is the transformation of field components. This step is realized by inserting a grid attribute object U, which is called a matrix transformation. For magnetization in the *Z*-direction, U takes the following form:

$$U = \frac{1}{\sqrt{2}} \begin{pmatrix} 1 & i & 0 \\ 1 & -i & 0 \\ 0 & 0 & \sqrt{2} \end{pmatrix} \quad (5)$$

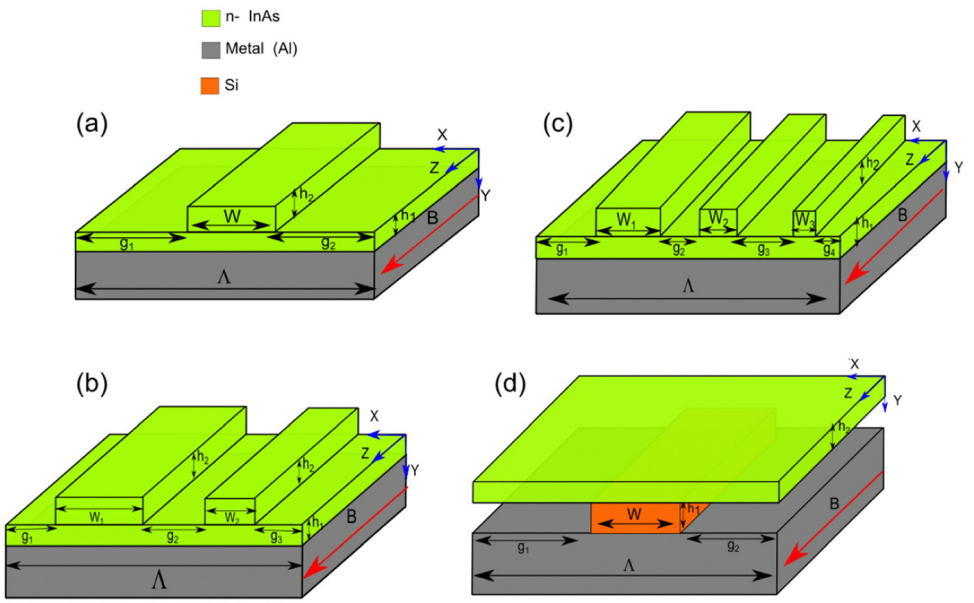

Fig. 3 Schematic of the proposed structures for violation of detailed balance or Kirchhoff's law at different angles of incidence. The first three structures (a–c) consist of (from top to bottom) a magneto-optical InAS grating, a magneto-optical film made of InAs, and an Al substrate. The fourth design (d) has Si as a sandwiched layer between the top magneto-optical film made of InAs and the bottom optically thick Al metal layer as the substrate. The incident wave is TM polarized with an electric field in the *x*–*y* plane, and an external magnetic field is applied in the *z*-direction. Using these four proposed designs, Tables 1–4 list the optimized parameters for different polar angles. We used the variables *W*, *g*, *h*, and Λ to describe the width, the gap between adjacent gratings, the height, and the period of the gratings, respectively.

The third step involves establishing contact between the anisotropic material created and the geometry drawn in the model. This can be accomplished by simply adding the Faraday attribute to the "grid attribute name" in the object's properties.

3. Results and discussion

3.1 Proposed metasurface design and optimization

In Fig. 3, all four metasurface designs are shown to demonstrate the proposed angle sensor. All the four structures had three layers. In the first three designs, the top layer is made up of n-doped InAs gratings, followed by a continuous layer of InAs, and the bottom layer is made up of optically thick aluminum (Al) metal to ensure no transmission. Guided mode resonance is the basis for these designs. The fourth design involves silicon (Si) as an important coupling dielectric medium between the grating layer on top and the bottom layer of optically thick Al.[53] In each of the four designs, the magnetic field B is applied to the z-axis (Voigt geometry), propagating along the y-axis, and periodic in the x-direction. The geometric parameters are as follows: Λ represents the period of the grating, h_1 and h_2 represent the thickness of the continuous layer of InAs and the grating, respectively, W represents the grating width in all designs, and g is the gap between two consecutive gratings. Tables 1, 2, 3 and 4 present designs 1, 2, 3 and 4, respectively. They provide all optimized parameters of designs and the corresponding angles. The permittivity tensor for InAs is given by the following expression:[45]

$$\varepsilon = \begin{pmatrix} \varepsilon_\infty - \dfrac{\omega_p^2(\omega+i\gamma)}{\omega\left[(\omega+i\gamma)^2-\omega_c^2\right]} & \dfrac{i\omega_p^2\omega_c}{\omega\left[(\omega+i\gamma)^2-\omega_c^2\right]} & 0 \\ -\dfrac{\omega_p^2(\omega+i\gamma)}{\omega\left[(\omega+i\gamma)^2-\omega_c^2\right]} & \varepsilon_\infty - \dfrac{\omega_p^2(\omega+i\gamma)}{\omega\left[(\omega+i\gamma)^2-\omega_c^2\right]} & 0 \\ 0 & 0 & \varepsilon_\infty - \dfrac{\omega_p^2}{\omega(\omega+i\gamma)} \end{pmatrix} \quad (6)$$

where ε_∞ = 13.7 is the permittivity at high frequency and ω is the angular frequency of the incident THz wave. $\gamma = \frac{1}{\tau} = 1.55 \times 10^{11}\ \mathrm{rad\ s^{-1}}$ is the relaxation rate (τ is the relaxation time), which depends on the experimental absorption of the materials.[45] $\omega_p = \sqrt{\frac{Ne^2}{\varepsilon_0 m^*}}$ is the plasma frequency, where N = $7.8 \times 10^{17}\ \mathrm{cm^{-3}}$ is the doping concentration, m^* = $0.33m_e$ (m_e is the electron mass), ε_0 is the free space permittivity and e^- is the elementary charge. The cyclotron frequency $\omega_c = \frac{eB}{m^*}$, where B is the external magnetic field intensity. The doping concentration N is higher than the intrinsic carrier concentration even at higher temperatures. Hence, the Drude model is expected to hold and ignore the effect of Landau quantization at room temperature, $k_B T \gg \frac{h}{2\pi}\omega_c$. The permittivity tensor in eqn (6) suggests that reciprocity is broken because the off-diagonal components and ε_{xy} are not equal to the ε_{yx} component, *i.e.*, $\varepsilon_{xy} \neq \varepsilon_{yx}$. The magneto-optic effect in InAs becomes stronger for larger values of $\frac{|\varepsilon_{xy}|}{|\varepsilon_{yx}|}$.[54] The nine designs are represented in Tables 1–4.

Table 1 Parameters for design 1 (Fig. 3a)

	Design 1					
Polar angle (θ)	Λ (μm)	W (μm)	g_1 (μm)	g_2 (μm)	h_1 (μm)	h_2 (μm)
−6	7.25	6	0.75	0.75	1	2.2
50	7.4	3.3	2.05	2.05	0.5	1.09

Table 2 Parameters for design 2 (Fig. 3b)

	Design 2							
Polar angle (θ)	Λ (μm)	W_1 (μm)	W_2 (μm)	g_1 (μm)	g_2 (μm)	g_3 (μm)	h_1 (μm)	h_2 (μm)
6	7.25	3	1	1.125	1.2	0.925	1	2.2
−33	7.25	1.5	0.5	1.875	1.7	1.175	1	2.2
20	7.25	4	0.9	1.025	0.35	0.975	1	2.2
−20	7.25	3	1.75	0.525	1.125	0.65	1	2.2
40	7.4	4	1	0.2	1.5	0.7	0.5	1

Table 3 Parameters for design 3 (Fig. 3d)

	Design 3									
Polar angle (θ)	Λ (μm)	W_1 (μm)	W_2 (μm)	W_3 (μm)	g_1 (μm)	g_2 (μm)	g_3 (μm)	g_4 (μm)	h_1 (μm)	h_2 (μm)
33	7.25	2.2	0.5	0.5	0.825	1.075	1.9	0.25	1	2.2
−50	7.25	3.3	0.5	0.5	0.55	0.325	1.9	0.325	0.5	1

Table 4 Parameters for design 4 (Fig. 4d)

	Design 4					
Polar angle (θ)	Λ (μm)	W (μm)	g_1 (μm)	g_2 (μm)	h_1 (μm)	h_2 (μm)
−46	7	2.46	2.27	2.27	0.2	1.3

3.2 Simulation results and angle sensor

Our next step is to analyze the results after summarizing the optimized geometric parameters of the proposed designs, as shown in Tables 1–4. The permittivity tensor in eqn (6) ε for n-InAs is diagonalized by a unitary matrix transformation U, *i.e.*,

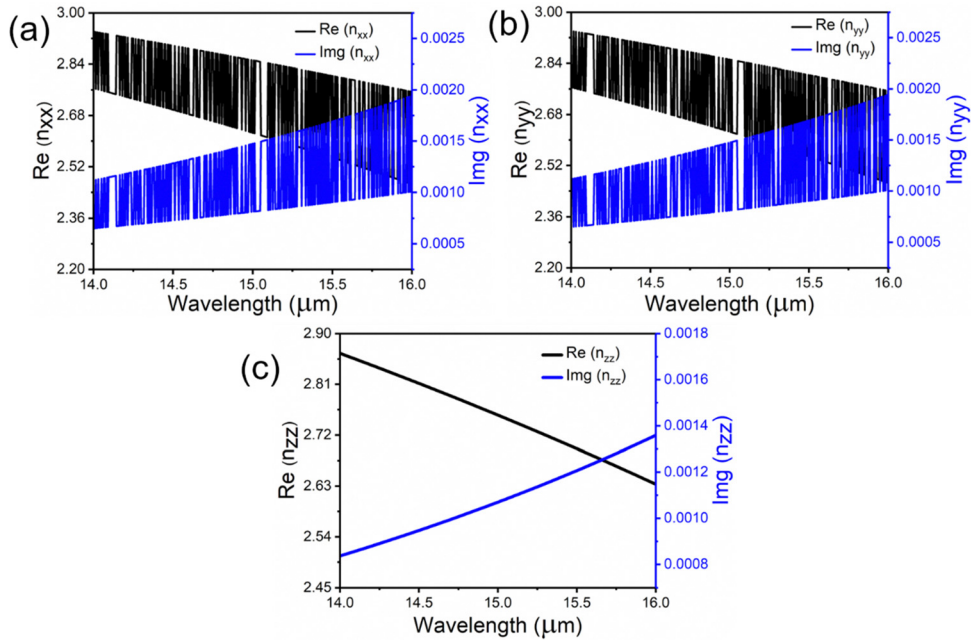

Fig. 4 Refractive index n of n-InAs under a magnetic field B = 3 T. (a) In x direction, (b) in y direction and (c) in z direction.

by treating it as a plane-symmetric tensor. The dielectric constant can be approximated by

$$\tilde{\varepsilon}_{\mathrm{D}} = U^{*} \cdot \tilde{\varepsilon} \cdot U = \begin{pmatrix} \varepsilon_{xx} & 0 & 0 \\ 0 & \varepsilon_{yy} & 0 \\ 0 & 0 & \varepsilon_{zz} \end{pmatrix} = \begin{pmatrix} {n_{xx}}^2 & 0 & 0 \\ 0 & {n_{yy}}^2 & 0 \\ 0 & 0 & {n_{zz}}^2 \end{pmatrix} \tag{7}$$

Fig. 4 shows the equivalent refractive index for n-InAs under a 3 T magnetic field, for the x, y, and z directions. As shown in Fig. 4(a) and (b), in the $x(n_{xx})$ and $y(n_{yy})$ directions, the refractive index fluctuates sharply. The analysis in Fig. 4 reveals a fluctuation in the refractive index along the midpoint line, indicating the impact of the magnetic field, which induces material anisotropy and dispersion.[50,55] Specifically, the magnetic field, aligned with the z-axis, solely influences the dielectric constant in the x–y plane, affecting the dielectric function tensors ε_{xx} and ε_{yy}. Consequently, this magnetic field has no impact on the refractive index n_{zz} in the z-direction, resulting in a constant refractive index irrespective of the magnetic field strength, as shown in Fig. 4(c). This observation highlights the anisotropic and dispersive nature of the material induced by a magnetic field, which has implications for its optical properties.

To demonstrate the ability of the complete metasurface array to act as an angle sensor, we first demonstrate the absorption and emission response from reciprocal and nonreciprocal metasurfaces with or without broken symmetry varying with the incident angle for metasurface design no. 1. Because the substrate is sufficiently optically thick, the transmission is zero ($T(\theta) = 0$). The absorption $\alpha(\theta)$ and emission $\varepsilon(\theta)$ as functions of the incident angle θ can be calculated as follows:[45]

$$\alpha(\theta) = 1 - R(\theta)$$

$$\alpha(-\theta) = 1 - R(-\theta)$$

and

$$\varepsilon(\theta) = 1 - R(-\theta)$$

$$\varepsilon(-\theta) = 1 - R(\theta)$$

where R is the reflectivity. As simulated in Fig. 5, for the reciprocal metasurface $\alpha(\theta) = \varepsilon(\theta) = \alpha(-\theta) = \varepsilon(-\theta)$, for the nonreciprocal metasurface $\alpha(\theta) \neq \varepsilon(-\theta)$, and for the nonreciprocal with nonsymmetric metasurface, $\alpha(\theta) \neq \varepsilon(-\theta)$. In our design, the incident light is TM polarized because no nonreciprocal effect can be created using light without TM polarization. An external magnetic field B is applied along the grating Z-axis, which corresponds to the Voigt geometry. In our design, Λ is set to be sufficiently large so that only one specular reflection occurs. The metasurface consists of a reciprocal material, symmetric in the k_x space, *i.e.*, $\omega(k_x) = \omega(-k_x)$.[56] Accordingly, the resonance angle is symmetric with respect to the normal, *i.e.*, $\theta = 0^{\circ}$. This results in $\alpha(\theta) = \varepsilon(\theta) = \alpha(-\theta) = \varepsilon(-\theta)$ and a detailed balance is satisfied, as shown in Fig. 5(a) and (b). Fig. 5(a) shows the case in which no external magnetic field B is applied and the metasurface is mirror-symmetric ($g_1 = g_2$). The absorption and emission curves follow each other and overlap perfectly, as shown in Fig. 5(b). As soon as an external magnetic field is applied to a magneto-optic material InAs, the photonic band structure in the k_x space exhibits asymmetry, *i.e.*, $\omega(k_x) \neq \omega(-k_x)$. Therefore, the resonance condition is not symmetric

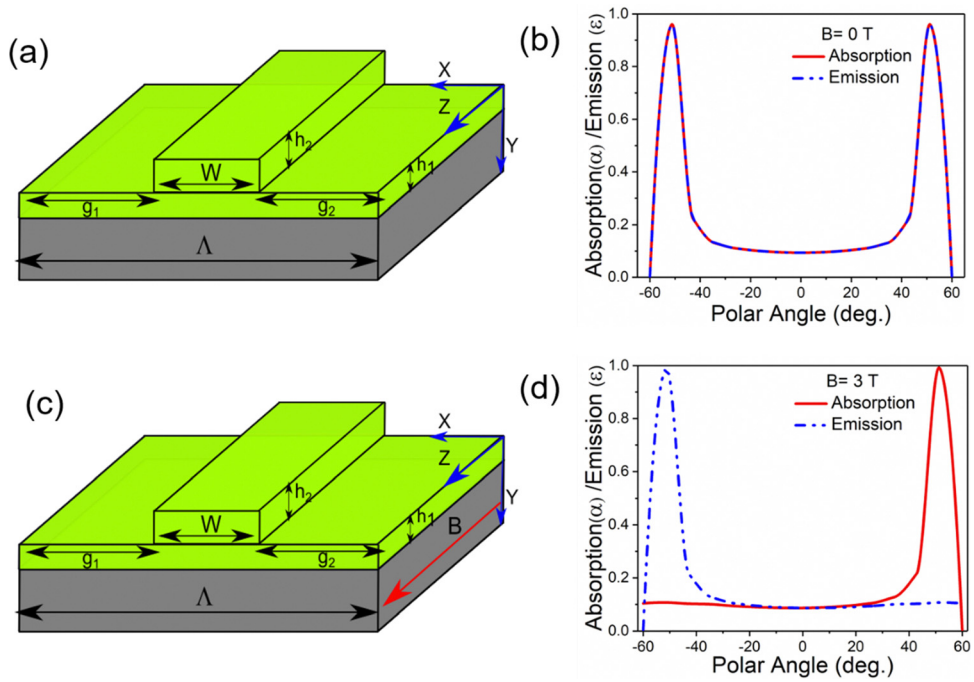

Fig. 5 Comparison of reciprocal and nonreciprocal angle sensors in terms of absorption as a function of polar angle or angle of incidence. (a) Schematic of one of the proposed optical metasurfaces used as an angle sensor. The angle sensor comprises an n-InAs metasurface and a uniform layer on a metal (Al). Light propagation is in the *y*-direction while the sensor is periodic in the *x*-direction, (b) showing typical absorption and emission profile in case of reciprocal metasurface. (c) A magnetic field (*B*) is applied in the *Z*-direction (red arrow) in a Voigt configuration (non-reciprocal metasurface) and (d) corresponding absorption and emission profile in case of non-reciprocal metasurface.

with respect to $\theta = 0^\circ$ and the detailed balance is violated. Fig. 5(c) illustrates the condition in which an external magnetic field is applied in the *Z*-direction and the gap between two consecutive InAs grooves is the same ($g_1 = g_2$). The absorption and emission are no longer symmetric with respect to $\theta = 0^\circ$ and the absorption occurs at a particular angle in the entire range from $+50^\circ$ to -50°, as shown in Fig. 5(d). The resonance can also be explained by the coupled mode theory, according to which the critical coupling condition is achieved when the intrinsic loss rate (γ_i) equals the external loss rate (γ_e).[45,57]

Then, we perform the same calculations on absorption as a function of the polar angle for the nine meta-surfaces in Tables 1–4. As illustrated in Fig. 6, each metasurface has different resonance angles and is optimized at 13 μm in the atmospheric window. Combining all nine proposed metasurface designs into an array allows the determination of the incoming radiation direction and camouflage as the emission direction is different from the incoming radiation direction. Fig. 6 shows the absorption *versus* polar angle for all nine metasurfaces listed in Tables 1–4 for the following angles: -50°, -46°, -33°, -20°, -6°, 6°, 20°, 33°, 40° and 50°.

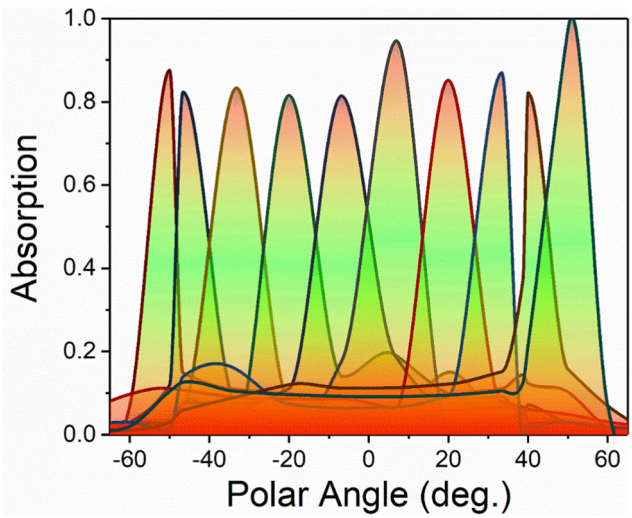

Fig. 6 Absorption as a function of polar angles for all non-reciprocal optimized designs in Tables 1–4 for the following angles: -50°, -46°, -33°, -20°, -6°, 6°, 20°, 33°, 40° and 50°.

4. Conclusion and outlook

We propose a set of nonreciprocal metasurfaces made of magneto-optic InAs materials in an array to detect the direction of incoming radiation and camouflaging due to $\alpha(\omega,\theta,\varphi) \neq \varepsilon(\omega,\theta,\varphi)$ followed by a nonreciprocal system. We designed and optimized nine metasurfaces working at different polar angles of -50°, -46°, -33°, -20°, -6°, 6°, 20°, 33°, 40° and 50°. The absorption bands in all cases showed greater than 80% absorption. A system such as this can conceivably be used for solar-energy harvesting system efficiency and thermal management. Using our design, nonreciprocal thermal emitters that are viable for practical applications can be constructed.

The promising capabilities of non-reciprocal metasurfaces open exciting avenues for advancing solar light harvesting and radiative cooling technologies.[58,59] In the realm of solar light harvesting, the distinctive absorption and emission profiles of non-reciprocal metasurfaces offer a unique advantage. By strategically designing metasurfaces that preferentially absorb sunlight from specific angles and emit thermal radiation in a controlled manner, these surfaces can significantly enhance the efficiency of solar cells. The non-reciprocal nature allows for tailored absorption characteristics, addressing variations in incident angles throughout the day and optimizing energy capture. Moreover, in the domain of radiative cooling, non-reciprocal metasurfaces present an innovative approach for modulating thermal emissions. These metasurfaces can be engineered to enhance the radiative cooling efficiency by exploiting the asymmetry between absorption and emission profiles. This has the potential to create surfaces that selectively emit thermal radiation to cold outer space, even in the presence of solar irradiance, facilitating passive cooling without the need for energy-intensive mechanisms. Research on non-reciprocal metasurfaces could explore multifunctional designs that simultaneously enhance solar light harvesting and radiative cooling. Integrating these surfaces into energy-efficient systems has the potential to revolutionize sustainable energy practices by improving the performance of solar cells and enabling passive cooling solutions. As we delve into these possibilities, the interdisciplinary applications of non-reciprocal metasurfaces are poised to redefine the landscape of renewable energy technologies.

Conflicts of interest

There are no conflicts to declare.

Acknowledgements

This work is supported by the research on interference optimization of cellular networks based on the intelligent reflecting surface project of the science and technology research program of the Chongqing Education Commission of China (no. KJQN202203101).

References

1 C. W. J. Beenakker, Thermal radiation and amplified spontaneous emission from a random medium, *Phys. Rev. Lett.*, 1998, **81**, 1829–1832, DOI: **10.1103/PhysRevLett.81.1829**.
2 C. Luo, A. Narayanaswamy, G. Chen and J. D. Joannopoulos, Thermal radiation from photonic crystals: A direct calculation, *Phys. Rev. Lett.*, 2004, **93**, 19–22, DOI: **10.1103/PhysRevLett.93.213905**.
3 Z. J. Coppens and J. G. Valentine, Spatial and Temporal Modulation of Thermal Emission, *Adv. Mater.*, 2017, **29**, 1–6, DOI: **10.1002/adma.201701275**.
4 S. K. Chamoli and W. Li, Visibly transparent multifunctional camouflage coating with efficient thermal management, *Opt. Lett.*, 2023, **48**, 4340, DOI: **10.1364/ol.494539**.
5 H. Zhu, Q. Li, C. Zheng, Y. Hong, Z. Xu, H. Wang, W. Shen, S. Kaur, P. Ghosh and M. Qiu, High-temperature infrared camouflage with efficient thermal management, *Light: Sci. Appl.*, 2020, **9**, DOI: **10.1038/s41377-020-0300-5**.
6 Y. Qu, Q. Li, L. Cai, M. Pan, P. Ghosh, K. Du and M. Qiu, Thermal camouflage based on the phase-changing material GST, *Light: Sci. Appl.*, 2018, **7**, 26, DOI: **10.1038/s41377-018-0038-5**.
7 D. Jung, S. Bank, M. L. Lee and D. Wasserman, Next-generation mid-infrared sources, *J. Opt.*, 2017, **19**, 123001, DOI: **10.1088/2040-8986/aa939b**.
8 W. Streyer, K. Feng, Y. Zhong, A. J. Hoffman and D. Wasserman, Selective absorbers and thermal emitters for far-infrared wavelengths, *Appl. Phys. Lett.*, 2015, **107**, 1–6, DOI: **10.1063/1.4929432**.
9 J.-H. Park, Holographic techniques for augmented reality and virtual reality near-eye displays, *Light: Advanced Manufacturing*, 2022, **3**, 9, DOI: **10.37188/lam.2022.009**.
10 L. Huang, Z. Hong, Q.-D. Chen, Y.-L. Zhang, S. Zhao, Y. Dong and Y.-Q. Liu, Imaging/nonimaging microoptical elements and stereoscopic systems based on femtosecond laser direct writing, *Light: Advanced Manufacturing*, 2023, **4**, 37, DOI: **10.37188/lam.2023.037**.
11 G. C. Hulley, R. M. Duren, F. M. Hopkins, S. J. Hook, N. Vance, P. Guillevic, W. R. Johnson, B. T. Eng, J. M. Mihaly, V. M. Jovanovic, S. L. Chazanoff, Z. K. Staniszewski, L. Kuai, J. Worden, C. Frankenberg, G. Rivera, A. D. Aubrey, C. E. Miller, N. K. Malakar, J. M. S. Tomás and K. T. Holmes, High spatial resolution imaging of methane and other trace gases with the airborne Hyperspectral Thermal Emission Spectrometer (HyTES), *Atmos. Meas. Tech.*, 2016, **9**, 2393–2408, DOI: **10.5194/amt-9-2393-2016**.
12 Y. Gong, S. S. Oh, D. L. Huffaker and N. Copner, Novel Mid-Infrared Metamaterial Thermal Emitters for Optical Gas Sensing, *Opt. Soc. Am., J.*, 2018, JTu3A.89, DOI: **10.1364/fio.2018.jtu3a.89**.
13 K. Du, Q. Li, Y. Lyu, J. Ding, Y. Lu, Z. Cheng and M. Qiu, Control over emissivity of zero-static-power thermal emitters based on phase changing material GST, *Light: Sci. Appl.*, 2017, **6**, e16194, DOI: **10.1038/lsa.2016.194**.
14 T. Kim, E. S. Yu, Y. G. Bae, J. Lee, I. S. Kim, S. Chung, S. Y. Lee and Y. S. Ryu, Asymmetric optical camouflage: tuneable reflective colour accompanied by the optical Janus effect, *Light: Sci. Appl.*, 2020, **9**, 175, DOI: **10.1038/s41377-020-00413-5**.
15 N. Baranwal and S. P. Mahulikar, Infrared signature of aircraft engine with choked converging nozzle, *J. Thermophys. Heat Transf.*, 2016, **30**, 854–862, DOI: **10.2514/1.T4641**.
16 X. Xie, X. Li, M. Pu, X. Ma, K. Liu, Y. Guo and X. Luo, Plasmonic Metasurfaces for Simultaneous Thermal Infrared Invisibility and Holographic Illusion, *Adv. Funct. Mater.*, 2018, **28**, DOI: **10.1002/adfm.201706673**.
17 L. Phan, W. G. Walkup IV, D. D. Ordinario, E. Karshalev, J. M. Jocson, A. M. Burke and A. A. Gorodetsky, Reconfigurable infrared camouflage coatings from a cephalopod

protein, *Adv. Mater.*, 2013, **25**, 5621–5625, DOI: **10.1002/adma.201301472**.

18 C. Xu, G. T. Stiubianu and A. A. Gorodetsky, Adaptive infrared-reflecting systems inspired by cephalopods, *Science*, 2018, **359**, 1495–1500, DOI: **10.1126/science.aar5191**.

19 O. Salihoglu, H. B. Uzlu, O. Yakar, S. Aas, O. Balci, N. Kakenov, S. Balci, S. Olcum, S. Süzer and C. Kocabas, Graphene-Based Adaptive Thermal Camouflage, *Nano Lett.*, 2018, **18**, 4541–4548, DOI: **10.1021/acs.nanolett.8b01746**.

20 M. J. Moghimi, G. Lin and H. Jiang, Broadband and Ultrathin Infrared Stealth Sheets, *Adv. Eng. Mater.*, 2018, **20**, DOI: **10.1002/adem.201800038**.

21 L. Xiao, H. Ma, J. Liu, W. Zhao, Y. Jia, Q. Zhao, K. Liu, Y. Wu, Y. Wei, S. Fan and K. Jiang, Fast Adaptive Thermal Camouflage Based on Flexible VO2/Graphene/CNT Thin Films, *Nano Lett.*, 2015, **15**, 8365–8370, DOI: **10.1021/acs.nanolett.5b04090**.

22 J. Song, S. Huang, Y. Ma, Q. Cheng, R. Hu and X. Luo, Radiative metasurface for thermal camouflage, illusion and messaging, *Opt. Express*, 2020, **28**, 875, DOI: **10.1364/oe.378424**.

23 B. Chen, S. Yang, J. Chen, J. Wu, K. Chen, W. Li, Y. Tan, Z. Wang, H. Qiu, K. Fan, C. Zhang, H. Wang, Y. Feng, Y. He, B. Jin, X. Wu, J. Chen and P. Wu, Directional terahertz holography with thermally active Janus metasurface, *Light: Sci. Appl.*, 2023, **12**, 136, DOI: **10.1038/s41377-023-01177-4**.

24 M. X. Ren, W. Wu, W. Cai, B. Pi, X. Z. Zhang and J. J. Xu, Reconfigurable metasurfaces that enable light polarization control by light, *Light: Sci. Appl.*, 2017, **6**, e16254, DOI: **10.1038/lsa.2016.254**.

25 M. Pu, X. Li, X. Ma, Y. Wang, Z. Zhao, C. Wang, C. Hu, P. Gao, C. Huang, H. Ren, X. Li, F. Qin, J. Yang, M. Gu, M. Hong and X. Luo, Catenary optics for achromatic generation of perfect optical angular momentum, *Sci. Adv.*, 2015, **1**, 1–7, DOI: **10.1126/sciadv.1500396**.

26 X. Luo, Principles of electromagnetic waves in metasurfaces, *Sci. China: Phys., Mech. Astron.*, 2015, **58**, 594201.

27 X. Wang and Z. Jacob, Symmetry breaking in thermal photonics, *Light: Sci. Appl.*, 2022, **11**, 10–11, DOI: **10.1038/s41377-022-01044-8**.

28 Y. Yang, J. Seong, M. Choi, J. Park, G. Kim, H. Kim, J. Jeong, C. Jung, J. Kim, G. Jeon, K. il Lee, D. H. Yoon and J. Rho, Integrated metasurfaces for re-envisioning a near-future disruptive optical platform, *Light: Sci. Appl.*, 2023, **12**, 152, DOI: **10.1038/s41377-023-01169-4**.

29 A. Basiri, X. Chen, J. Bai, P. Amrollahi, J. Carpenter, Z. Holman, C. Wang and Y. Yao, Nature-inspired chiral metasurfaces for circular polarization detection and full-Stokes polarimetric measurements, *Light: Sci. Appl.*, 2019, **8**, 78, DOI: **10.1038/s41377-019-0184-4**.

30 M. Liu, W. Zhu, P. Huo, L. Feng, M. Song, C. Zhang, L. Chen, H. J. Lezec, Y. Lu, A. Agrawal and T. Xu, Multifunctional metasurfaces enabled by simultaneous and independent control of phase and amplitude for orthogonal polarization states, *Light: Sci. Appl.*, 2021, **10**, 107, DOI: **10.1038/s41377-021-00552-3**.

31 C. Yan, K. Y. Yang and O. J. F. Martin, Fano-resonance-assisted metasurface for color routing, *Light: Sci. Appl.*, 2017, **6**, e17017, DOI: **10.1038/LSA.2017.17**.

32 L. Huang, *Breaking the spatial reciprocity with Janus metamaterials*, Springer, US, 2019, DOI: **10.1038/s41377-019-0175-5**.

33 H. Gao, X. Fan, W. Xiong and M. Hong, Recent advances in optical dynamic meta-holography, *Opto-Electron. Adv.*, 2021, **4**, 210030, DOI: **10.29026/oea.2021.210030**.

34 Y. Guo, S. Zhang, M. Pu, Q. He, J. Jin, M. Xu, Y. Zhang, P. Gao and X. Luo, Spin-decoupled metasurface for simultaneous detection of spin and orbital angular momenta via momentum transformation, *Light: Sci. Appl.*, 2021, **10**, DOI: **10.1038/s41377-021-00497-7**.

35 X. Guo, Y. Ding and Y. Duan, Nonreciprocal metasurface with space–time phase modulation, *Light: Sci. Appl.*, 2019, **8**, 123.

36 S. K. Chamoli, M. ElKabbash and C. Guo, Switchable Gratings for Ultracompact and Ultrahigh Modulation Depth Plasmonic Switches, *Plasmonics*, 2022, **17**, 1361–1368, DOI: **10.1007/s11468-022-01602-1**.

37 S. K. Chamoli, G. Verma, S. C. Singh and C. Guo, Phase change material based hot electron photodetection, *Nanoscale*, 2021, **13**, 1311–1317, DOI: **10.1039/d0nr06456d**.

38 Y. Zhu, X. Zang, H. Chi, Y. Zhou, Y. Zhu and S. Zhuang, Metasurfaces designed by a bidirectional deep neural network and iterative algorithm for generating quantitative field distributions, *Light: Advanced Manufacturing*, 2023, **4**, 9, DOI: **10.37188/lam.2023.009**.

39 K. Zangeneh Kamali, L. Xu and N. Gagrani, Electrically programmable solid-state metasurfaces via flash localised heating, *Light: Sci. Appl.*, 2023, **12**, 40, DOI: **10.1038/s41377-023-01078-6**.

40 G. Huang, K. Wang and C. N. Markides, Efficiency limits of concentrating spectral-splitting hybrid photovoltaic-thermal (PV-T) solar collectors and systems, *Light: Sci. Appl.*, 2021, **10**, 28, DOI: **10.1038/s41377-021-00465-1**.

41 Z. Xu, H. Luo, H. Zhu, Y. Hong, W. Shen, J. Ding, S. Kaur, P. Ghosh, M. Qiu and Q. Li, Nonvolatile Optically Reconfigurable Radiative Metasurface with Visible Tunability for Anticounterfeiting, *Nano Lett.*, 2021, **21**, 5269–5276, DOI: **10.1021/acs.nanolett.1c01396**.

42 G. Kirchhoff, *Ann. Phys. Chem.*, 1860, **109**, 275.

43 C. Khandekar and Z. Jacob, New spin-resolved thermal radiation laws for nonreciprocal bianisotropic media, Opt. InfoBase Conf. Pap, 2021, DOI: **10.1364/noma.2021.nom1e.5**.

44 B. Zhao, Y. Shi, J. Wang, Z. Zhao, N. Zhao and S. Fan, Near-complete violation of Kirchhoff's law of thermal radiation with a 03 T magnetic field, *Opt. Lett.*, 2019, **44**, 4203, DOI: **10.1364/ol.44.004203**.

45 L. Zhu, Near-complete violation of detailed balance in thermal radiation, *Phys. Rev. B: Condens. Matter Mater. Phys.*, 2014, **90**(1–5), 220301, DOI: **10.1103/PhysRevB.90.220301**.

46 Y. Park, V. S. Asadchy, B. Zhao, C. Guo, J. Wang and S. Fan, Violating Kirchhoff's Law of Thermal Radiation in Semitransparent Structures, *ACS Photonics*, 2021, **8**, 2417–2424, DOI: **10.1021/acsphotonics.1c00612**.

47 J. Wu, R. Zeng, J. Liang, L. Jiang and Y. Xiang, Tunable GH shifts in Weyl thin films on a Weyl substrate, *J. Appl. Phys.*, 2021, **129**, 153103, DOI: **10.1063/5.0043579**.

48 S. Chamoli, W. Li, F. Mechanics and M. Elkabbash, Angularly selective thermal emitters for deep subfreezing daytime radiative cooling, *Nanophotonics*, 2022, **11**(16), 3709–3717, DOI: **10.1515/nanoph-2022-0032**.

49 G. A. Rao and S. P. Mahulikar, Effect of atmospheric transmission and radiance on aircraft infrared signatures, *J. Aircr.*, 2005, **42**, 1046–1054, DOI: **10.2514/1.7515**.

50 H. Wang, H. Wu and Z. Shen, Nonreciprocal optical properties of thermal radiation with SiC grating magneto-optical materials, *Opt. Express*, 2017, **25**, 19609, DOI: **10.1364/oe.25.019609**.

51 V. S. Asadchy, C. Guo, B. Zhao and S. Fan, Sub-Wavelength Passive Optical Isolators Using Photonic Structures Based on Weyl Semimetals, *Adv. Opt. Mater.*, 2020, **8**, 36–39, DOI: **10.1002/adom.202000100**.

52 B. Zhao, C. Guo, C. A. C. Garcia, P. Narang and S. Fan, Axion-Field-Enabled Nonreciprocal Thermal Radiation in Weyl Semimetals, *Nano Lett.*, 2020, **20**, 1923–1927, DOI: **10.1021/acs.nanolett.9b05179**.

53 X. Wu, Z. Chen and F. Wu, Strong Nonreciprocal Radiation in a InAs Film by Critical Coupling with a Dielectric Grating, *ES Energy Environ.*, 2021, **13**, 8–12, DOI: **10.30919/esee8c442**.

54 X. Luo, M. Zhou, J. Liu, T. Qiu, Z. Yu, X. Luo, M. Zhou, J. Liu, T. Qiu and Z. Yu, Magneto-optical metamaterials with extraordinarily strong magneto-optical effect, *Appl. Phys. Lett.*, 2016, **108**, 131104, DOI: **10.1063/1.4945051**.

55 H. Wang, H. Wu and J. Qiu Zhou, Nonreciprocal optical properties based on magneto-optical materials: n-InAs, GaAs and HgCdTe, *J. Quant. Spectrosc. Radiat. Transfer*, 2018, **206**, 254–259, DOI: **10.1016/j.jqsrt.2017.11.015**.

56 R. D. M. J. D. Joannopoulos, S. G. Johnson and J. N. Winn, *Photonic Crystals: Molding the Flow of Light*, Princeton University Press, Princeton, NJ, 2nd edn, 2011.

57 B. Zhao, J. Wang, Z. Zhao, C. Guo, Z. Yu and S. Fan, Nonreciprocal Thermal Emitters Using Metasurfaces with Multiple Diffraction Channels, *Phys. Rev. Appl.*, 2021, **16**, 1, DOI: **10.1103/PhysRevApplied.16.064001**.

58 C. He, Y. Shen and A. Forbes, Towards higher-dimensional structured light, *Light: Sci. Appl.*, 2022, **11**, 205, DOI: **10.1038/s41377-022-00897-3**.

59 M. Lee, G. Kim, Y. Jung, K. R. Pyun, J. Lee, B. Kim and S. H. Ko, Photonic structures in radiative cooling, *Light: Sci. Appl.*, 2023, **12**, 134, DOI: **10.1038/s41377-023-01119-0**.

